

REPORT DOCUMENTATION PAGE			Form Approved OMB NO. 0704-0188		
<p>The public reporting burden for this collection of information is estimated to average 1 hour per response, including the time for reviewing instructions, searching existing data sources, gathering and maintaining the data needed, and completing and reviewing the collection of information. Send comments regarding this burden estimate or any other aspect of this collection of information, including suggestions for reducing this burden, to Washington Headquarters Services, Directorate for Information Operations and Reports, 1215 Jefferson Davis Highway, Suite 1204, Arlington VA, 22202-4302. Respondents should be aware that notwithstanding any other provision of law, no person shall be subject to any penalty for failing to comply with a collection of information if it does not display a currently valid OMB control number.</p> <p>PLEASE DO NOT RETURN YOUR FORM TO THE ABOVE ADDRESS.</p>					
1. REPORT DATE (DD-MM-YYYY)		2. REPORT TYPE New Reprint		3. DATES COVERED (From - To) -	
4. TITLE AND SUBTITLE Computational Analysis and Experimental Validation of the Ti-6Al-4V Friction Stir Welding Behavior			5a. CONTRACT NUMBER W911NF-11-1-0207		
			5b. GRANT NUMBER		
			5c. PROGRAM ELEMENT NUMBER 622105		
6. AUTHORS M. Grujicic, G. Arakere, B. Pandurangan, A. Hariharan, C-F.Yen, B. A. Cheeseman, C. Fountzoulas			5d. PROJECT NUMBER		
			5e. TASK NUMBER		
			5f. WORK UNIT NUMBER		
7. PERFORMING ORGANIZATION NAMES AND ADDRESSES Clemson University Office of Sponsored Programs 300 Brackett Hall, Box 345702 Clemson, SC 29634 -5702				8. PERFORMING ORGANIZATION REPORT NUMBER	
9. SPONSORING/MONITORING AGENCY NAME(S) AND ADDRESS(ES) U.S. Army Research Office P.O. Box 12211 Research Triangle Park, NC 27709-2211				10. SPONSOR/MONITOR'S ACRONYM(S) ARO	
				11. SPONSOR/MONITOR'S REPORT NUMBER(S) 57228-EG.19	
12. DISTRIBUTION AVAILABILITY STATEMENT Approved for public release; distribution is unlimited.					
13. SUPPLEMENTARY NOTES The views, opinions and/or findings contained in this report are those of the author(s) and should not be construed as an official Department of the Army position, policy or decision, unless so designated by other documentation.					
14. ABSTRACT A fully coupled thermomechanical finite element analysis of the friction-stir welding (FSW) process developed in the authors' previous work is combined with the basic physical metallurgy of Ti-6Al-4V to predict/assess the structural response of FSW joints. A close examination of the experimental results reported in the open literature reveals that in most cases the heat-affected zone (HAZ) of the weld possesses the most inferior properties and tends to control the overall structural performance of the weld. Taking this observation into account, a microstructure					
15. SUBJECT TERMS friction-stir welding, Ti-6Al-4V, finite element analysis, weld microstructure/properties prediction					
16. SECURITY CLASSIFICATION OF:			17. LIMITATION OF ABSTRACT UU	15. NUMBER OF PAGES	19a. NAME OF RESPONSIBLE PERSON Mica Grujicic
a. REPORT UU	b. ABSTRACT UU	c. THIS PAGE UU			19b. TELEPHONE NUMBER 864-656-5639

## **Report Title**

Computational Analysis and Experimental Validation of the Ti-6Al-4V Friction Stir Welding Behavior

### **ABSTRACT**

A fully coupled thermomechanical finite element analysis of the friction-stir welding (FSW) process developed in the authors' previous work is combined with the basic physical metallurgy of Ti-6Al-4V to predict/assess the structural response of FSW joints. A close examination of the experimental results reported in the open literature reveals that in most cases the heat-affected zone (HAZ) of the weld possesses the most inferior properties and tends to control the overall structural performance of the weld. Taking this observation into account, a microstructure evolution model is developed and parameterized for the Ti-6Al-4V material residing in the HAZ. Specifically, this model addresses the problem of temporal evolution of the globular  $\alpha$ -phase particles located within prior  $\beta$ -phase grains (the dominant microstructural parameter in the HAZ) during the FSW process. Next this model is combined with the well-established property versus microstructure correlations in Ti-6Al-4V in order to predict the overall structural performance of the weld. The results obtained are found to be in reasonably good agreement with their experimental counterparts, suggesting that the present computational approach may be used to guide the selection of FSW process parameters in order to optimize the structural performance of FSW joints (at least while they are controlled by the HAZ-material microstructure/properties).

---

**REPORT DOCUMENTATION PAGE (SF298)**  
**(Continuation Sheet)**

---

Continuation for Block 13

ARO Report Number     57228.19-EG  
Computational Analysis and Experimental Valida     ...

Block 13: Supplementary Note

© 2011 . Published in Proceedings of the Institution of Mechanical Engineers, Part B: Journal of Engineering Manufacture, Vol. Ed. 0 225, (2) (2011), (, (2). DoD Components reserve a royalty-free, nonexclusive and irrevocable right to reproduce, publish, or otherwise use the work for Federal purposes, and to authroize others to do so (DODGARS §32.36). The views, opinions and/or findings contained in this report are those of the author(s) and should not be construed as an official Department of the Army position, policy or decision, unless so designated by other documentation.

Approved for public release; distribution is unlimited.

# Proceedings of the Institution of Mechanical Engineers, Part B: Journal of Engineering Manufacture

<http://pib.sagepub.com/>

---

## Computational analysis and experimental validation of the friction-stir welding behaviour of Ti—6Al—4V

M Grujicic, G Arakere, B Pandurangan, A Hariharan, B A Cheeseman, C-F Yen and C Fountzoulas  
*Proceedings of the Institution of Mechanical Engineers, Part B: Journal of Engineering Manufacture* 2011 225: 208  
DOI: 10.1177/09544054JEM2013

The online version of this article can be found at:  
<http://pib.sagepub.com/content/225/2/208>

---

Published by:



<http://www.sagepublications.com>

On behalf of:



[Institution of Mechanical Engineers](#)

Additional services and information for *Proceedings of the Institution of Mechanical Engineers, Part B: Journal of Engineering Manufacture* can be found at:

Email Alerts: <http://pib.sagepub.com/cgi/alerts>

Subscriptions: <http://pib.sagepub.com/subscriptions>

Reprints: <http://www.sagepub.com/journalsReprints.nav>

Permissions: <http://www.sagepub.com/journalsPermissions.nav>

Citations: <http://pib.sagepub.com/content/225/2/208.refs.html>

>> [Version of Record](#) - Feb 1, 2011

[What is This?](#)

# Computational analysis and experimental validation of the friction-stir welding behaviour of Ti-6Al-4V

M Grujicic<sup>1\*</sup>, G Arakere<sup>1</sup>, B Pandurangan<sup>1</sup>, A Hariharan<sup>1</sup>, B A Cheeseman<sup>2</sup>, C-F Yen<sup>2</sup>, and C Fountzoulas<sup>2</sup>

<sup>1</sup>Department of Mechanical Engineering, Clemson University, Clemson, South Carolina, USA

<sup>2</sup>Army Research Laboratory – Survivability Materials Branch, Aberdeen, Maryland, USA

*The manuscript was received on 5 February 2010 and was accepted after revision for publication on 4 May 2010.*

DOI: 10.1177/09544054JEM2013

**Abstract:** A fully coupled thermomechanical finite element analysis of the friction-stir welding (FSW) process developed in the authors' previous work is combined with the basic physical metallurgy of Ti-6Al-4V to predict/assess the structural response of FSW joints. A close examination of the experimental results reported in the open literature reveals that in most cases the heat-affected zone (HAZ) of the weld possesses the most inferior properties and tends to control the overall structural performance of the weld. Taking this observation into account, a microstructure evolution model is developed and parameterized for the Ti-6Al-4V material residing in the HAZ. Specifically, this model addresses the problem of temporal evolution of the globular  $\alpha$ -phase particles located within prior  $\beta$ -phase grains (the dominant microstructural parameter in the HAZ) during the FSW process. Next this model is combined with the well-established property versus microstructure correlations in Ti-6Al-4V in order to predict the overall structural performance of the weld. The results obtained are found to be in reasonably good agreement with their experimental counterparts, suggesting that the present computational approach may be used to guide the selection of FSW process parameters in order to optimize the structural performance of FSW joints (at least while they are controlled by the HAZ-material microstructure/properties).

**Keywords:** friction-stir welding, Ti-6Al-4V, finite element analysis, weld microstructure/properties prediction

## 1 INTRODUCTION

Friction-stir welding (FSW) is a solid-state joining process that was invented in 1991 by Thomas *et al.* at The Welding Institute in the UK [1]. The basic concept behind the FSW process for the case of butt welding is displayed schematically in Fig. 1. Essentially, a non-consumable rotating tool (Fig. 2) consisting of a pin (usually conically shaped and containing threads, flutes, and flats) and a shoulder (usually containing scrolls or spirals) is forced to move along the contacting surfaces of two rigidly butt-clamped plates (the workpiece). Heat dissipation associated with frictional sliding at the shoulder/workpiece and pin/workpiece interfaces, as well as

plastic deformation caused by the rotating and advancing tool, causes the workpiece material to soften to a temperature near the respective solidus temperature. This, in turn, enables the tool to stir the surrounding material, causing its extrusion around the tool and forging in the wake of the tool. Since the tool is rotating as it traverses along the butted surfaces, the FSW process is essentially asymmetric, i.e. one typically makes a distinction between the so-called 'advancing side' of the weld (the side on which the peripheral velocity of the rotating tool coincides with the transverse velocity of the tool) and the 'retreating side' (the side on which the two velocities are aligned in the opposite directions).

FSW normally involves complex interactions and competition between various mass and heat transport phenomena, plastic deformation and damage/fracture mechanisms, and microstructure evolution processes [2–9]. Consequently, the material microstructure

\*Corresponding author: Department of Mechanical Engineering, Clemson University, 241 EIB, Clemson, SC 29634, USA.  
email: mica@ces.clemson.edu

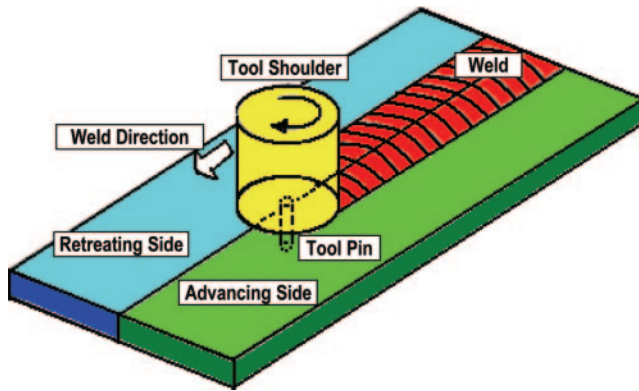


Fig. 1 Schematic illustration of the FSW process

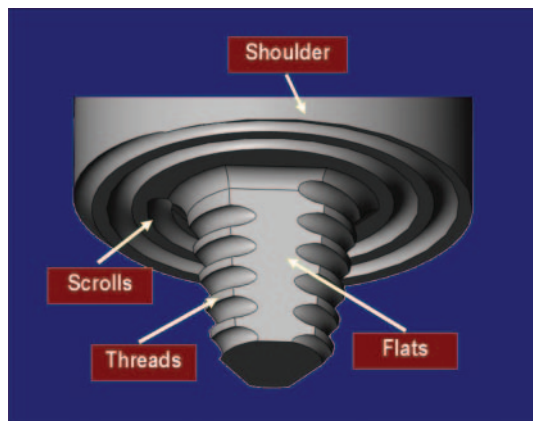


Fig. 2 Typical FSW tool used for joining high-melting-temperature titanium-alloy grades

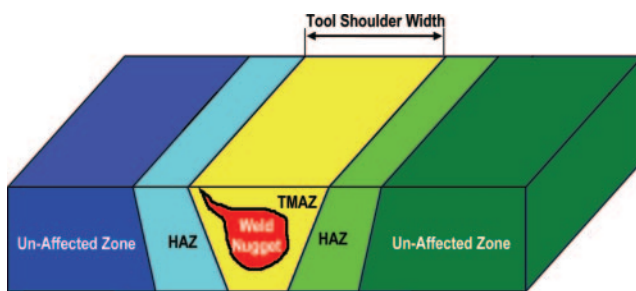


Fig. 3 Schematic illustration of the main microstructural zones associated with the typical FSW joint

(and mechanical properties) in the weld region are highly complex and spatially diverse. Metallographic examinations of FSW joints typically reveal the existence of the following four zones (see Fig. 3).

1. An unaffected (base metal) zone which is far enough from the weld so that material microstructure/properties are not altered by the joining process.
2. A heat-affected zone (HAZ) in which material microstructure/properties are affected only by the thermal effects associated with FSW. While this

zone is normally found in the case of fusion welds, the nature of the microstructural changes may be different in the FSW case due to generally lower temperatures and a more diffuse heat source.

3. A thermomechanically affected zone (TMAZ) which is located closer than the HAZ zone to the butting surfaces. Consequently, both the thermal and the mechanical aspects of the FSW process affect the material microstructure/properties in this zone. Typically, the original grains are retained in this zone although they may have undergone severe plastic deformation.
4. A weld nugget, which is the innermost zone of an FSW joint. As a result of the way the material is transported from the regions ahead of the tool to the wake regions behind the tool, this zone typically contains so-called 'onion-ring' features. The material in this region has been subjected to the most severe conditions of plastic deformation and high-temperature exposure, and consequently contains a very fine, dynamically recrystallized (equiaxed grain) microstructure.

Relative to traditional fusion-welding technologies, FSW offers a number of advantages. Since a fairly detailed discussion pertaining to these advantages can be found in the authors' recent work [10], a similar detailed account is not given here. Instead, it should be noted that most of these advantages arise from the fact that FSW is associated with lower temperatures, does not involve fusion and re-solidification of the weld material, and that no filler metal, flux, or fuel/oxidizer is used.

Despite the fact that FSW was discovered less than 20 years ago, this joining process has found wide-scale application in many industries. Among the most notable examples in which full advantage of the FSW process was taken to reduce production cost and fabricate durable structures are:

- (a) FSW is being used in serial production of aluminium alloy-based ferryboat deck structures in Finland;
- (b) Al-Mg-Si alloy-based bullet-train cabins are commonly fabricated in Japan using FSW as the primary joining process;
- (c) Boeing predominantly utilizes FSW in the manufacture of Al-Cu alloy-based rocket-launch systems;
- (d) NASA has almost completely replaced conventional fusion-welding processes with FSW for critical joints in the space shuttle's external fuel tanks, which are manufactured using Al-Li alloy;
- (e) General Electric has begun to use FSW in very demanding jet engine applications.

Due to their relatively high specific strength/stiffness (typically 40 to 50 per cent higher than that of



steels) and superior erosion/corrosion resistance, titanium and its alloys have been traditionally widely used in the aerospace, chemical, and nuclear industries. Additional important reasons for the wide acceptance of titanium and its alloys include:

- (a) non-magnetic character;
- (b) ability to be fabricated using conventional processing methods;
- (c) availability in a variety of fabricated forms (such as plates, sheets, rods, pipes, wires, extrusions, stampings, castings, forgings, powders, and superplastic forms);
- (d) reasonable affordability.

In recent years, titanium and its alloys have increasingly been employed by the defence industry for various armour applications. One of the primary reasons for the increased interest in titanium and its alloys is a commitment by the military to attain air-transportable and rapidly deployable forces. Due to their lower density, higher specific strength/stiffness, and superior blast/ballistic resistance, titanium and its alloys hold the potential for significantly reducing the weight of military vehicles without compromising their blast and IED (improvised explosive device) survivability. It is estimated that a 5–6 per cent reduction in the weight of a military vehicle typically increases its air-transportable range on average by 200 miles. Superior ballistic performance of titanium and its alloys is another important reason for the increased use of these materials in military applications. For light to medium class armoured vehicles, a common ballistic resistance requirement includes a superior combination of survivability with respect to fragment and kinetic energy threats. Titanium and its alloys generally provide a quite attractive resistance to fragment and kinetic energy threats. For example, Ti-6Al-4V (the alloy studied in the present work) shows ballistic resistance to a 20 mm fragment-simulating projectile comparable to that found in AA5083 (an aluminium alloy grade commonly employed in ballistic armour applications) and clearly outperforms rolled homogeneous armour (RHA). In addition, Ti-6Al-4V outperforms both AA5083 and RHA with respect to resistance to the 14.5 mm BS32 kinetic energy-round. A literature review carried out as part of the present work revealed that the military has been aware of the low density and superior ballistic resistance offered by titanium and its alloys for quite some time. The main reasons for the early reluctance by the military to employ these materials in tactical and battle-field vehicles are:

- (a) unfamiliarity with the processing and fabrication behaviour of this material;
- (b) a not fully founded belief of prohibitively high cost;
- (c) lesser emphasis of the military on low-weighting of its fleet and unwillingness to pay a high premium for the benefits offered by titanium and its alloys.

Titanium and its alloys have been joined traditionally using conventional fusion-welding techniques such as gas tungsten arc welding (GTAW), gas metal arc welding (GMAW), electron beam welding (EBW), plasma arc welding (PAW), and laser beam welding (LBW). Commonly, the use of these welding processes for joining titanium and its alloys is accompanied by various problems related to the formation of a brittle cast microstructure within the weld, severe weldment distortions, and high residual stresses. To overcome these problems, the feasibility of joining titanium and its alloys using various solid-state joining technologies (e.g. diffusion bonding, explosive welding, etc.) has been investigated in recent years. A brief overview of the main efforts related to the use of one of these solid-state joining techniques, i.e. FSW, for joining titanium and its alloys is provided below.

A detailed literature review, carried out within the present work, pertaining to the use of FSW for the joining of titanium and its alloys revealed the following main research and development efforts. The early efforts were focused on demonstrating FSW feasibility for titanium and its alloys and on characterizing the resulting weld microstructure and properties. For example in 2003, Ramirez and Juhas [11] successfully applied the FSW process to Ti-6Al-4V and carried out a detailed microstructural investigation of the different weld zones. In the same time period, John *et al.* [12] carried out a detailed investigation of the near-threshold fatigue crack growth properties in Ti-6Al-4V FSW joints and demonstrated that residual stresses within the welds play a critical role in controlling the fatigue crack growth rate. In 2005, Lee *et al.* [13] demonstrated FSW feasibility in the case of commercial-purity titanium and carried out a detailed examination of the microstructure and mechanical properties of the weld. That work also clearly revealed the challenges associated with the design of and material selection for FSW tools in the case of high-melting-temperature and high-strength workpiece materials like titanium. Specifically, it was shown that due to high attendant temperatures these tools have to be made of high-temperature hard materials such as titanium carbide. Around the same period, Reynolds *et al.* [14] examined the feasibility of FSW for a prototypical  $\beta$ -type titanium alloy and examined the resulting microstructure evolution (including the texture evolution) within different weld zones during the FSW process. In 2007, Fonda *et al.* [15] demonstrated the FSW feasibility for Ti-5-1-1-1 (a titanium alloy

containing 5 per cent Al, 1 per cent Sn, 1 per cent Zr, 1 per cent V, and 0.8 per cent Mo) and carried out a detailed investigation of the material's microstructure within different weld zones. In the most recent investigations of the FSW joining of titanium and its alloys, the emphasis is being placed mainly on establishing correlations between the FSW process parameters and the resulting weld microstructure and properties. For example in 2007, Zhang *et al.* [16] investigated the effect of FSW process parameters (specifically, a varying tool rotational speed at a constant level of tool traverse speed and a constant tool-workpiece contact pressure) on the microstructure and (hardness and tensile) properties in Ti-6Al-4V FSW welds. In 2009, Liu *et al.* [17] extended the work of Zhang *et al.* to include the effect of varying tool traverse speeds on the weld microstructure and properties.

The main objective of the present work is to combine the fully coupled thermomechanical finite element analysis of the FSW process, developed in the authors' previous work [18, 19], with the basic physical metallurgy of Ti-6Al-4V. The operation and interaction of various microstructure evolution processes taking place during FSW of Ti-6Al-4V (e.g. extensive plastic deformation, dynamic recrystallization, globularization or dissolution of the primary  $\alpha$ -phase, formation of  $\alpha/\beta$  lamellar colonies, etc.) is considered to predict the material microstructure/properties in the various FSW zones.

The organization of the paper is as follows. The key physical metallurgy aspects of Ti-6Al-4V are reviewed in section 2. The FSW behaviour of the alloy is discussed in section 3. The fully coupled thermomechanical analysis used in the computational investigation of the FSW process is presented in section 4. A comparison between the computational results and their experimental counterparts pertaining to the as friction-stir welded microstructure and properties of the welds is presented in section 5. The main conclusions resulting from the present study are summarized in section 6.

## 2 PHYSICAL METALLURGY OF Ti-6Al-4V

Before one can expect to successfully complete the task of understanding the effect of FSW process parameters on the material microstructure and properties in different zones of a Ti-6Al-4V weld, it is critical that a reasonably good understanding of the physical metallurgy of this alloy be acquired. Specifically, one should become familiar with all the stable and meta-stable phases present in this alloy system, the thermal (and mechanical) conditions under which these phases are formed, and the effect of the material's thermal-mechanical history on its micro-

structure, as well as the basic correlations between the phases present, their morphologies, and the resulting material properties. In the remainder of this section, a brief overview of these aspects of the Ti-6Al-4V physical metallurgy is provided.

Pure titanium undergoes, during heating, an allotropic phase transformation from a low-temperature, hexagonal-close-packed  $\alpha$ -phase to the high-temperature, body-centred-cubic  $\beta$ -phase at a ('beta transus') temperature of 882.5 °C. Alloying elements can thermodynamically stabilize either the  $\alpha$ - or  $\beta$ -phase, i.e. increase or decrease the beta-transus temperature (range). Consequently, titanium alloys may contain at room temperature different relative amounts of the two phases and are typically classified as  $\alpha$ -type,  $\alpha + \beta$ -type, and  $\beta$ -type alloys. Among titanium alloys,  $\alpha + \beta$ -type are of particular interest since vastly different mechanical properties can be imparted through the use of various thermomechanical treatments.

Ti-6Al-4V alloy analysed in the present work falls into the category of  $\alpha + \beta$ -type titanium alloys. This alloy is generally considered as the workhorse of the titanium industry and accounts for more than 50 per cent of the total titanium consumption. The alloy offers a good overall combination of the properties such as low density, high strength/stiffness, reasonably good corrosion resistance, good hot-warm and cold formability, and superior weldability with respect to fusion-based welding techniques. The maximum service temperature for Ti-6Al-4V alloy is generally quoted as 350 °C.

To obtain different combinations of material properties in Ti-6Al-4V, the following heat treatments are most often employed.

1. *Mill annealing*, consisting of a high-temperature soaking treatment within the  $\alpha + \beta$ - or  $\beta$ -phase region followed by air cooling. The primary purpose of this (often incomplete) heat treatment is to remove heavily deformed microstructures resulting from cold/warm working.
2. *Recrystallization annealing*, consisting of a sufficiently long soaking treatment in the high-temperature portion of the  $\alpha + \beta$ -phase region followed by slow cooling.
3. *Beta-annealing*, same as the recrystallization annealing except that the soaking is done in the single  $\beta$ -phase region. Both recrystallization and beta-annealing treatments improve material fracture toughness.
4. *Stabilization annealing*, same as the recrystallization annealing except that the soaking is done in the lower-temperature portion of the  $\alpha + \beta$ -phase region. This results in an increased partitioning of the  $\beta$ -phase-stabilizing elements to the



$\beta$ -phase, reducing the probability for formation of an embrittling meta-stable  $\omega$ -phase.

5. *Stress-relief annealing*, same as the stabilization annealing except that soaking is carried out over a shorter time period which is sufficient to relieve generally undesirable residual stresses via dislocation recovery/polygonization processes without measurably affecting material strength/ductility.
6. *Vacuum annealing*, the main purpose of this heat treatment is to 'de-gas' the alloy, i.e. to remove deleterious interstitial elements/contaminants such as oxygen, hydrogen and nitrogen.
7. *Solution treatment plus ageing*, involving high-temperature soaking in the  $\beta$ -phase (and sometimes in the  $\alpha + \beta$ -phase) region followed by water quenching to room temperature and ageing at an intermediate temperature.

Heat treatments like the ones just discussed are used to alter the material microstructure and, in turn, mechanical properties of the alloy. While only two phases ( $\alpha$  and  $\beta$ ) are normally observed in this alloy, the aforementioned heat treatments can produce vastly different microstructures/properties. Despite the fact that this alloy has been used for over 30 years, a complete knowledge of the basic microstructure/property relationships is still lacking. Nevertheless, some of these relationships are well established and are explained below. To aid this discussion, a schematic quasi-binary phase diagram is depicted in Fig. 4 in which the concentration of all alloying elements is represented by a single variable (an effective concentration) and defined along the  $x$ -axis.

When the alloy is soaked at a temperature exceeding the upper beta-transus line (e.g. point A in Fig. 4), it transforms completely to the  $\beta$ -phase; if the soaking temperature is too high and/or the soaking time is too long, it may suffer excessive grain growth (compromises quasi-static and dynamic strength). If the alloy is subsequently (air or furnace) cooled to room temperature (i.e. into the  $\alpha + \beta$ -region) a portion of the  $\beta$ -phase will transform into the  $\alpha$ -phase (in the form of thin lamellae grouped to form well-defined  $\alpha + \beta$ -lamellar colonies within the  $\beta$ -phase matrix/grains), Fig. 5(a). This microstructural form of the  $\alpha$ -phase is beneficial with respect to the fracture toughness and stress corrosion cracking resistance of the material.

When the alloy is quenched from the  $\beta$ -phase soaking temperature, the  $\alpha$ -phase typically does not form and instead the  $\beta$ -phase transforms martensitically (i.e. without any segregation/partitioning of the alloying elements) into an orthorhombic meta-stable  $\alpha''$ -phase. During subsequent ageing at an intermediate temperature, the orthorhombic phase retransforms to a microstructure consisting of the  $\beta$ -phase matrix and fine equiaxed  $\alpha$ -phase pre-

cipitates, Fig. 5(b). This type of microstructure is generally found to improve the material's low- and high-cycle fatigue strength as well as its fracture toughness.

When high-temperature soaking of the alloy is carried out within the  $\alpha + \beta$ -phase region (e.g. point B in Fig. 4), the final microstructure contains the so-called 'primary  $\alpha$ -phase particles'. These particles are thermodynamically stable since they are formed as a result of material annealing in the two-phase region. The primary  $\alpha$ -phase particles are generally globular in shape and, since they form along the  $\beta$ -phase grain boundaries, they play a beneficial role in preventing excessive  $\beta$ -phase grain growth. During subsequent cooling to room temperature, additional  $\alpha$ -phase is formed whose morphology depends on the cooling rate in the same way as that observed in the case of the alloy soaked in the  $\beta$ -phase region, Figs 5(c) and (d). It should be noted that smaller  $\beta$ -phase grains are depicted in Figs 5(c) and (d) relative to those depicted in Figs 5(a) and (b) in order to graphically represent the beneficial role of primary  $\alpha$ -phase particles in inhibiting  $\beta$ -phase grain growth. The presence of the primary  $\alpha$ -phase particles and the resulting smaller-size  $\beta$ -phase grains and  $\alpha + \beta$  colonies are typically found to improve the material's fracture toughness and creep resistance. It should also be noted that soaking in the  $\alpha + \beta$ -phase region results in the formation of a more stable  $\beta$ -phase (i.e.  $\beta$ -phase with a higher amount of  $\beta$ -stabilizing vanadium). This, in turn, can be beneficial since it reduces the tendency for formation of another meta-stable and highly embrittling phase, the  $\omega$ -phase.

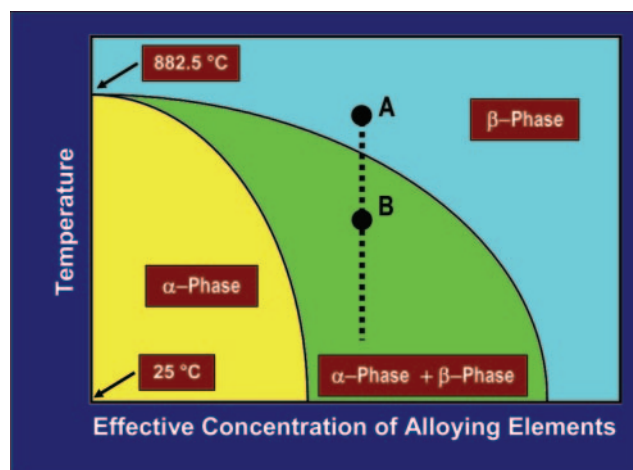


**Fig. 4** Schematic of the titanium-based quasi-binary phase diagram in which the concentration of all alloying elements is lumped into a single quantity termed 'effective concentration of alloying elements'. The nominal chemistry of the  $\alpha + \beta$  Ti-6Al-4V alloy is indicated by the vertical dashed line

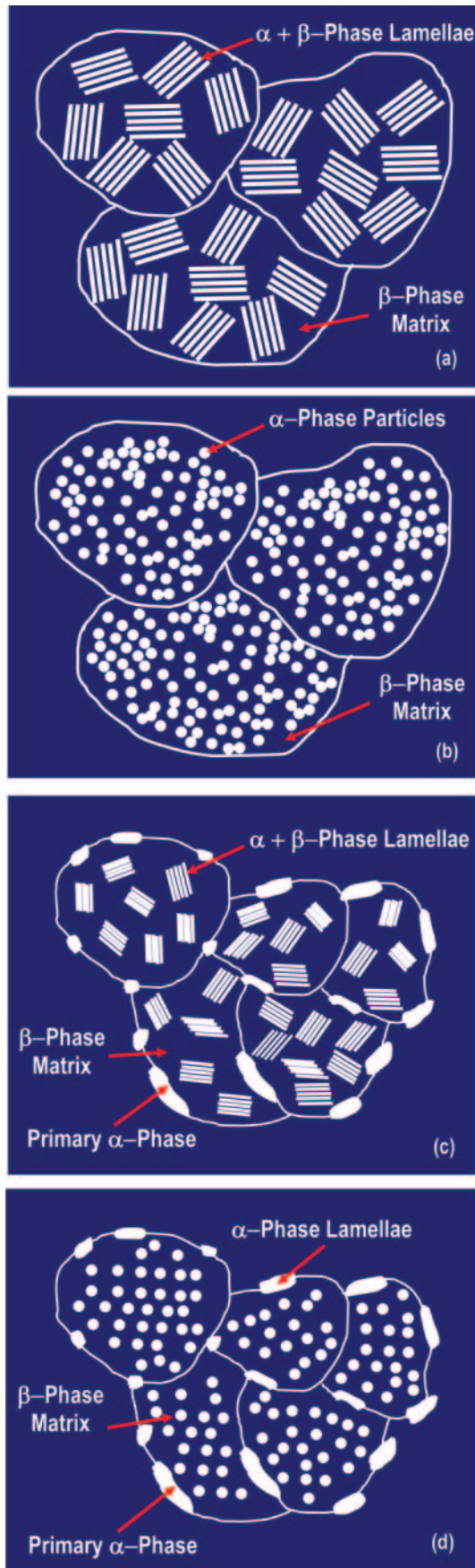


Fig. 5 Schematic representation of the Ti-6Al-4V material

### 3 FSW BEHAVIOUR OF Ti-6Al-4V

As mentioned in section 1, in contrast to the case of aluminium alloys, relatively fewer investigations of the FSW behaviour of titanium alloys (including Ti-6Al-4V) have been carried out. The literature review carried out as part of the present work established that the most comprehensive research regarding the FSW behaviour of Ti-6Al-4V was reported in references [16] and [19]. Consequently, in the remainder of this section a detailed yet concise summary is provided of the findings reported in these investigations.

The work reported in references [16] and [19] involved investigations of the effect of FSW process parameters (such as tool rotational speed, tool travel speed, tool design/material, workpiece thickness, downward contact pressure applied to the tool, tool tilt angle, pin plunge depth, shoulder plunge depth, coolant flow through the weld tool, and the coolant flow through the backing anvil) on the weld microstructure and properties. The weld microstructure and macrostructure were investigated using various optical and scanning electron microscopy techniques, while the weld properties were investigated using microhardness measurements, transverse and all-weld tensile testing techniques, as well as surface profilometry.

The main findings/observations made in references [16] and [19] can be summarized as follows.

1. For each workpiece thickness it is found that there is a unique combination of the optimal FSW process parameters with respect to the overall quality of the weld. An example of the optimal sets of FSW process parameters as reported in reference [20] is reproduced in Table 1.
2. Due to rotational and translational motion of the FSW tool shoulder relative to the workpiece, surface markings (also known as surface texture) are produced on the top surface of the weld. The extent of the resulting surface roughness as characterized by the arithmetic mean surface roughness, maximum peak-to-valley height, and the so-called 'ten-point height parameter' may seriously compromise the performance of the weld by causing stress concentration effects. Specifically, the fatigue life of the FSW weldment may be seriously compromised since the very sharp surface markings typically act as a source of crack initiation. To prevent this deleterious effect of surface texture, a generally unwanted secondary (machining) operation may need to be employed in order to remove the very top layer of the FSW weldment.
3. In comparison with the prototypical aluminium-alloy FSW joints, Ti-6Al-4V welds are found to

**Table 1** Summary of the optimal Ti-6Al-4V FSW process parameters [20]

Joint thickness (mm)	Spindle speed (r/min)	Travel speed (mm/min)	Shoulder diameter (mm)	Pin-tip diameter (mm)
3.0	300	50–130	20	8
6.0	250–320	45–100	25	10
9.0	250–285	65–100	25	10
12.0	140–190	40–75	30	10

possess an extremely small HAZ, with an average width of the order of 200–400  $\mu\text{m}$ . This finding is generally linked with the low thermal conductivity of titanium-based alloys.

4. In sharp contrast to the typical observations made in aluminium alloys, the TMAZ in Ti-6Al-4V is negligibly small and is usually hard to distinguish from the HAZ. This finding has been attributed to a combined effect of low thermal conductivity and high strength in Ti-6Al-4V. In other words, the lower extent of heat transfer from the stir zone (i.e. weld nugget) to the surrounding workpiece material leaves the latter material in the state of lower temperature and higher strength. This, in turn, limits the extent of plastic deformation in the surrounding material.
5. While, at any given depth, the grain/colony size distribution within the weld nugget is quite uniform, significant variations in these microstructural parameters are typically found at different depths. Since clearly coarser microstructures are observed in the crown region of the weld relative to the root region, these observations are linked with the relatively low thermal conductivity of the workpiece material and to the fact that a majority of the heat is generated at the shoulder/workpiece interface.
6. The workpiece thickness is found to have a profound effect on the coarseness of the weld microstructure. Since coarser microstructures are observed in thicker welds, this effect of the workpiece thickness has been linked with the associated cooling rates.
7. The HAZ typically contains the so-called 'bimodal microstructure', which consists of globular primary  $\alpha$ -phase particles (formed during high-temperature exposure of the material) and  $\alpha + \beta$ -lamellar colonies (formed during subsequent cooling) distributed within the  $\beta$ -phase matrix. This type of microstructure is an indication that the maximum temperature experienced by the material in this region does not exceed the upper beta-transus line. The workpiece thickness is not generally found to affect the material microstructure significantly in this weld zone.

**Fig. 6** Two most often observed FSW flaws: (a) voids; (b) incomplete welds

8. Except in the case of the smallest thickness (3 mm) workpiece, material microstructure in the stir zone is found not to contain any (globular) primary  $\alpha$ -phase suggesting that the workpiece material in this region is subjected to temperatures exceeding the upper beta-transus line. In addition, the smaller  $\beta$ -phase grains found in this region relative to those in the base metal suggests the interplay of dynamic recrystallization. Since the centre of the weld nugget typically contains somewhat coarser  $\beta$ -phase grains than the surrounding retreating and advancing sides of the weld, it appears that grain growth also plays a role in microstructure formation in the centre of the weld.
9. Material microhardness within the weld nugget is typically found to be affected by the workpiece thickness. That is, relative to the base material's microhardness levels, the microhardness of the weld nugget material is higher in the case of thinner workpieces and of comparable magnitude in the case of thick workpieces. This effect appears to be related to the aforementioned variation in the coarseness of the weld nugget's microstructure with the workpiece thickness.
10. Material microhardness in the HAZ is found to be generally lower than that in the base metal and not to be greatly affected by variations in the workpiece thickness.
11. The overall quality of the weld is found to be most affected by the relative and absolute values of the tool rotational and travel speeds. Specifically, tool rotational speed is found to control the rate of heat generation, while the tool travel speed normally influences the extent of material stirring at the weld root and the potential for the formation of flaws. The most common FSW flaws appear as voids (Fig. 6(a)) in the weld root and as



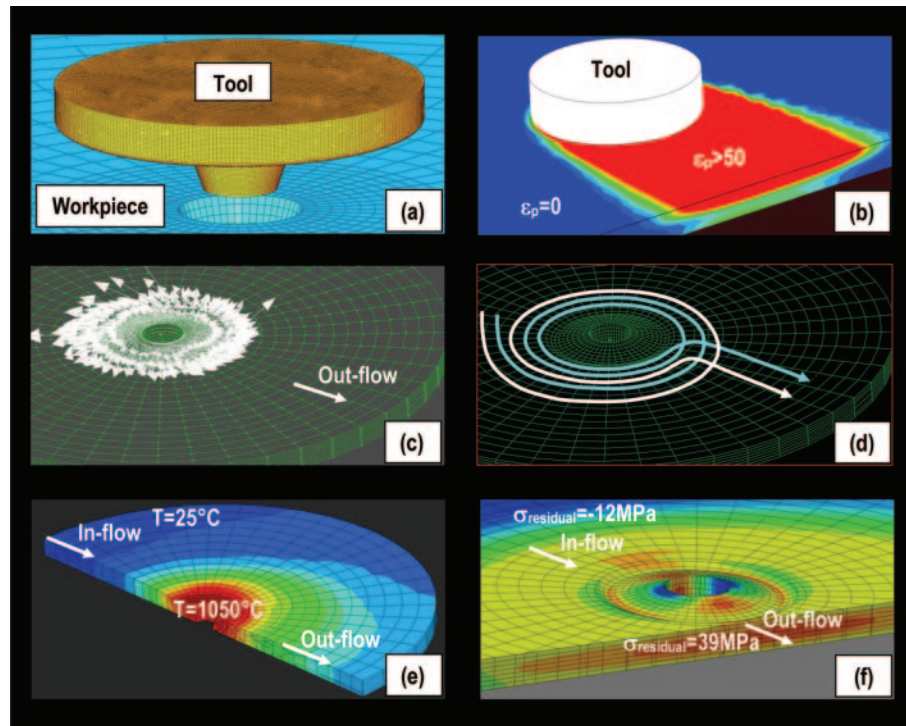


**Fig. 7** (a) Meshed models for the tool and the workpiece. Typical FSW computational analysis results pertaining to the steady-state distribution of: (b) equivalent plastic strain; (c) nodal velocities; (d) material-particle trajectories; (e) temperature; (f) residual stresses

welds not fully extending through the workpiece thickness (Fig. 6(b)), both caused by insufficient tool-pin plunging and incomplete material stirring.

#### 4 FSW COMPUTATIONAL ANALYSIS AND TYPICAL RESULTS

As mentioned in section 1, modelling of the FSW process carried out in the present work employed the fully coupled thermomechanical finite element procedure developed in the authors' prior work [18, 19]. Since a detailed account of the procedure has been provided in references [18] and [19], only the key aspects of this procedure are presented in the remainder of this section. Also, a brief overview of the workpiece and FSW-tool material models and the typical results obtained in FSW computational analysis are given in this section.

##### 4.1 FSW computational analysis

###### 4.1.1 Computational domain

The computational domain used consists of a (40.0 mm radius, 3.0 mm thickness) circular plate (with a concentric through-the-thickness conical hole, 5 mm radius on top and 3 mm radius on the bottom) and a two-part tool (consisting of a hole-

matching conical (flats-free and thread-free) pin and an 18 mm diameter solid right circular cylindrical shoulder), Fig. 7(a). The tool geometry was selected to match the one used in a companion experimental investigation of the FSW behaviour of Ti-6Al-4V. The computational domain is meshed using ~20 000 first-order eight-node, reduced-integration, hexahedral, thermomechanically coupled solid elements. The meshed model is displayed in Fig. 7(a); for clarity, the tool is shown in the retracted position.

###### 4.1.2 Computational analysis type

The FSW process is analysed computationally using a fully coupled thermomechanical finite element algorithm within which heat dissipation associated with plastic deformation and tool/workpiece interfacial friction-sliding is treated as a heat source in the governing thermal equation, while the effect of temperature on the mechanical response of the workpiece material is taken into account through the use of a temperature-dependent workpiece material model.

###### 4.1.3 Initial conditions

The analysis is carried out by prescribing from the onset a constant rotational speed, a zero tool translational speed along the butted surfaces, and a constant downward pressure to the tool. Since the tool is

not allowed to travel, the workpiece material is assigned the translational velocity of the tool but in the opposite direction. Thus, Fig. 7(a) represents not the entire workpiece but rather a circular region around the tool in the otherwise infinitely long/wide workpiece. Both the workpiece and the tool are initially set to the ambient temperature.

#### 4.1.4 Boundary conditions

To mimic the role played by the workpiece rigid backing plate in preventing flow of the workpiece material in the downwards direction, zero normal velocity boundary conditions are applied over the bottom surface of the workpiece. To comply with the requirement for a constant translational speed of the tool, the appropriate in-flow and out-flow velocities are prescribed over the circumferential portion of the workpiece surface (in a direction opposite to that of tool travel). Over the top portion of the workpiece as well as over the surface of its centre hole, the material normal velocities are set equal to their mesh counterparts. As far as the thermal boundary conditions are concerned, standard convective boundary conditions are applied over free surfaces of the workpiece and the tool while enhanced convection boundary conditions are applied over the bottom face of the workpiece (to mimic the effect of enhanced heat extraction through the workpiece backing plate).

#### 4.1.5 Tool/workpiece contact interactions

Workpiece/tool interactions are accounted for through the use of a penalty algorithm within which the extent of contact pressure is governed by the local surface penetrations, while shear stresses are transferred via a 'slip/stick' algorithm, i.e. shear stresses lower than the frictional shear stress are transferred without interface sliding (otherwise interface sliding takes place). The frictional shear stress is defined by a modified Coulomb law within which there is an upper limit to this quantity (set equal to the shear strength of the workpiece material). The frictional shear stress is then defined as the smaller of the product between the static/kinetic friction coefficient and the contact pressure, on the one hand, and the workpiece material shear strength, on the other.

#### 4.1.6 Heat generation and partitioning

As mentioned in section 4.1.2, both plastic deformation and frictional sliding are treated as heat sources. To account for the fact that a small fraction of the plastic deformation work is stored in the form of crystal defects, 95 per cent of this work is assumed to be dissipated in the form of heat. As far as heat generation due to frictional sliding is concerned, it is

assumed that its rate scales with the product of local interfacial shear stress and the sliding rate, and that 100 per cent of this energy is dissipated in the form of heat. Partitioning of this heat between the tool and the workpiece is then computed using the appropriate thermal properties of the two materials.

#### 4.1.7 Computational algorithm

As established earlier, workpiece material in the nugget and TMAZ regions experiences large plastic deformations during FSW. Under these circumstances, the use of a Lagrangian approach in which the finite element mesh is attached to and moves with the material may display serious numerical problems (due to excessive mesh distortion). To overcome this approach, an arbitrary Lagrangian Eulerian (ALE) formulation is used within which adaptive re-meshing is carried out to maintain good mesh quality. The fully coupled thermomechanical problem dealing with FSW is solved using an explicit solution algorithm implemented in ABAQUS/Explicit [21], a general-purpose finite element solver.

#### 4.1.8 Computational accuracy, stability, and cost

To keep the computational cost reasonable while ensuring accuracy and stability of the computational procedure, a mass scaling algorithm is used. This algorithm adaptively adjusts material density in the critical (time step-controlling) finite elements without significantly affecting the computational analysis results.

### 4.2 Material models

#### 4.2.1 Tool material

As mentioned in section 1, selecting the tool material for FSW of titanium alloys is quite challenging due to the high strength and low thermal conductivity of the workpiece material. Consequently, FSW tools are typically made of sintered advanced ceramic materials such as tungsten lanthanides or titanium carbides. Owing to the high strength of these materials, the tool does not typically suffer much deformation during the FSW process. However, tool wear may become a serious issue. Since an analysis of tool wear is beyond the scope of the present work, the tool material is considered as being rigid. Consequently, and considering the fact that the tool acquires a portion of the heat generated due to slip at the tool/workpiece interface, the thermal properties and density for the tool material still have to be specified. For the tungsten lanthanide tool material considered in the present work, the following properties were used: thermal conductivity  $k = 120$  W/m K, specific heat  $c_p = 140$  J/kg K, and density  $\rho = 18\,900$  kg/m<sup>3</sup>.

**Table 2** Material parameters in the Johnson–Cook yield strength model\* and the corresponding elastic and thermal parameters for Ti–6Al–4V

Parameter	Symbol	Units	Value
Reference strength	$A$	MPa	880.0
Strain-hardening parameter	$B$	MPa	695.0
Strain-hardening exponent	$n$	N/A	0.36
Strain-rate coefficient	$C$	N/A	0.04
Room temperature	$T_{\text{room}}$	K	293
Melting temperature	$T_{\text{melt}}$	K	3293.0
Temperature exponent	$m$	N/A	0.8
Young's modulus	$E$	GPa	113.8
Poisson's ratio	$\nu$	N/A	0.34
Density	$\rho$	kg/m <sup>3</sup>	4430
Thermal conductivity	$k$	W/m K	6
Specific heat	$c_p$	J/kg K	526

(N/A, not applicable.

\*  $\sigma_y = [A + B(\bar{\epsilon}^{\text{pl}})^n] [1 + C \log(\dot{\epsilon}^{\text{pl}}/\dot{\epsilon}_0^{\text{pl}})] [1 - T_H^m]$ , where  $\sigma_y$  is yield strength,  $\bar{\epsilon}^{\text{pl}}$  is equivalent plastic strain ( $\dot{\epsilon}_0^{\text{pl}}$ , initial value), and  $T_H$  is hardening temperature.)

#### 4.2.2 Workpiece material

The workpiece material (Ti–6Al–4V) is assumed to be an isotropic, linear-elastic and strain-hardenable, strain-rate-sensitive, thermally softenable plastic material and is modelled using the Johnson–Cook material model [22]. A summary of the Johnson–Cook material model parameters (including the governing equation for the yield stress,  $\sigma_y$ ) and the elastic and thermal properties of Ti–6Al–4V are provided in Table 2.

It should be noted that in the original Johnson–Cook material model, temperature affects the material strength only reversibly by promoting thermal activation of dislocation motion. In other words, no permanent changes in the material microstructure and properties are assumed to result from a high-temperature exposure of the material. This assumption is not fully justified in the case of FSW where it is commonly observed that high temperatures in the weld nugget give rise to dynamic recrystallization with an accompanying grain size refinement. To account for this additional effect of temperature, a modification to the original Johnson–Cook model was proposed in the authors' prior work [18, 19]. Essentially, strain hardening is still assumed to be related to the equivalent plastic strain  $\bar{\epsilon}^{\text{pl}}$  via a parabolic relationship:  $B(\bar{\epsilon}^{\text{pl}})^n$ , where  $B$  and  $n$  are material parameters (Table 2). However,  $\bar{\epsilon}^{\text{pl}}$  is taken now to be composed of two terms: one (positive) associated with the operation of plastic deformation and the other (negative) resulting from the operation of dynamic recrystallization. In other words, reduction in the dislocation density caused by dynamic recrystallization is modelled as an (apparent) effective reduction in the equivalent plastic strain, i.e. in the component of equivalent plastic

strain which is responsible for strain hardening. On the other hand, the total equivalent plastic strain, which measures the extent of irreversible overall deformation in the material, remains unaffected by dynamic recrystallization.

### 4.3 Typical results

In this section, a few typical computational results obtained using the Ti–6Al–4V FSW process analysis of section 4.2 are presented. Since similar results were obtained in the case of aluminium alloys AA5083 and AA2139 and are discussed in greater detail in a prior work [10], a similar detailed discussion of the Ti–6Al–4V results is not given here. Overall, the results presented in this section reveal correlations between the FSW process parameters (e.g. rotational and travel velocities of the tool, tool plunge depth, tool tilt angle, and tool design/material) and various field quantities (e.g. equivalent plastic strain, nodal velocities, and materials/particle velocities). It should be noted that all the results shown pertain to the steady-state FSW regime and not to the transient regime corresponding to the start-up of the FSW process.

#### 4.3.1 Equivalent plastic strain field

An example of the spatial distribution of the equivalent plastic strain in the workpiece during FSW is displayed in Fig. 7(b). Results like the ones shown in Fig. 7(b) can be used to assess the variation in the extent of plastic deformation in the transverse and through-the-thickness directions and link these with the overall quality and the properties of the weld. Examination of the equivalent plastic strain spatial distribution and temporal evolution results obtained in the present work (but not shown for brevity) reveals the following.

1. Depending on the FSW process conditions such as tool contact pressure and tool rotational and translational speeds, equivalent plastic strains in a range between 20 and 50 are observed.
2. The highest equivalent plastic strains are always found in the workpiece material right below the tool shoulder and decrease progressively from this region as a function of distance in the radial and through-the-thickness directions.
3. There is a highly pronounced asymmetry in the distribution of the equivalent plastic strain relative to the initial location of the butting surfaces. This asymmetry is related to the aforementioned differences in the material transport (at the advancing and the retreating sides of the weld) from the region ahead of the tool to the region behind the tool.



4. As the tool translational speed is decreased and the tool/workpiece contact pressure is increased, higher equivalent plastic strains are observed and equivalent plastic strain differences between the top and bottom surfaces of the workpiece are reduced. This finding suggests that under these FSW process conditions the extent of material stirring/mixing (which plays a critical role in weld quality/joint strength) is increased.

#### 4.3.2 Nodal velocity field

An example of the distribution of nodal velocities at the outer surfaces of the workpiece is displayed in Fig. 7(c); for clarity, the tool is not shown. Examination of the nodal velocity spatial distribution and temporal evolution results obtained in the present work (but not shown for brevity) reveals the following.

1. An initially assigned unidirectional velocity field in the direction of welding quickly transforms into the velocity field in which there is a well-defined stir region right below the shoulder (within which the material circles around the pin) and the remainder of the field (within which the material tends to flow around the stir region).
2. The region underneath the tool shoulder which is initially unfilled becomes filled as FSW proceeds. Once the space under the shoulder is fully filled it remains filled as the FSW process continues. The material in this region is constantly being refreshed as the tool advances in the welding direction.

#### 4.3.3 Material-particle trajectory field

It should be noted that, due to the ALE character of the finite element analysis used in the present work, the motion of the finite element mesh is not completely tied to the motion of the material. Hence, there is generally a disparity between nodal velocities and material-particle velocities. An example of the (colour-coded) traces left by two material particles as they approach the tool, enter the stir zone, and ultimately depart from the tool is displayed in Fig. 7(d). Results like the ones displayed in Fig. 7(d) can be used to assess the extent of material stirring and, in turn, to predict the quality of the weld. Examination of the material-particle trajectory results in the present work (but not shown for brevity) reveals the following.

1. The workpiece material at the retreating side does not, for the most part, enter the stir zone under the tool shoulder and usually only flows around it.
2. The material at the advancing side which is initially close to the butting surfaces passes over to the

retreating side and is co-stirred with some of the retreating-side material to form the welded joint.

3. The advancing-side material further away from the initial butting surfaces remains on the advancing side and either enters the stir region on the advancing side or flows around it.

#### 4.3.4 Temperature field

Typical spatial distribution of temperature over a medial longitudinal section of the workpiece is displayed in Fig. 7(e). Results like the ones displayed in Fig. 7(e) can be used in the FSW process optimization in order to ensure that the workpiece material has been sufficiently softened throughout the workpiece thickness (without being subjected to excessively high temperatures), which is a prerequisite for getting good-quality FSW joints.

Examination of the temperature spatial distribution and temporal evolution results obtained in the present work (but not shown for brevity) reveals the following.

1. Depending on the FSW process conditions such as tool contact pressure and tool rotational and translational speeds, temperatures in a range between 350 °C and 450 °C are obtained.
2. The highest temperatures are always found in the workpiece material right below the tool shoulder and the temperatures decrease progressively from this region as a function of distance in the radial and through-the-thickness directions.
3. As the tool rotational speed and contact pressure are increased, higher temperatures are observed and the temperature differences between the top and bottom surfaces of the workpiece are reduced.
4. By computing the energies dissipated via the plastic deformation process and that dissipated through frictional sliding at the tool/workpiece interfaces, it is found that plastic deformation typically contributes about 30 per cent to the overall heat generation; this contribution increases slowly with an increase in the translational velocity of the tool.

#### 4.3.5 Residual stress field

Due to non-uniformities in the extent of plastic deformation and temperature within the weld, FSW weldments often contain residual stresses. Since these stresses may significantly affect the structural and environmental resistance/durability of welded joints, it is critical that they are quantified and that their magnitudes and spatial distributions be correlated with various FSW process parameters. An example of the spatial distribution of the transverse

residual normal stresses over the medial longitudinal section of the workpiece is displayed in Fig. 7(f).

## 5 PREDICTION OF THE FSW JOINT STRUCTURAL PERFORMANCE

### 5.1 Weld quality versus weld-material microstructure/properties

As discussed in section 4, when assessing the success of the employment of the FSW process for joining Ti-6Al-4V structures, one is generally concerned both about the overall quality of the weld (as manifested by the absence of voids, incomplete joints, highly pronounced surface texture, and other flaws) as well as with the metallurgical state and the properties of the material in different zones of the weld (primarily in the HAZ and the stir zone). The computational analysis employed in the present work showed that if the FSW process parameters are properly selected, flaw-free FSW joints can be produced. Under such conditions, it is the metallurgical state/microstructure of the material in the weld that controls the overall structural performance of the weld. In this section, it is assumed that flaw-free FSW joints are indeed produced and then an attempt is made to assess/predict the microstructural state and the properties of the different weld zones, as well as of the FSW joint as a whole.

As mentioned in section 3, due to a relatively low thermal conductivity and a relatively high strength, Ti-6Al-4V welds do not contain a TMAZ of significant size. For the remaining two weld zones (the HAZ and the stir zone) the following was established previously.

#### 5.1.1 Heat-affected zone

This zone typically contains a bimodal room-temperature microstructure consisting of globular primary  $\alpha$ -phase particles located along grain boundaries of the prior  $\beta$ -phase grains and  $\alpha + \beta$ -lamellar colonies. This type of microstructure suggests that the material in the HAZ was never subjected to temperatures exceeding the upper beta-transus line. The microstructure parameters which have the dominant effect on the strength and ductility of the material with this type of microstructure are the globular  $\alpha$ -phase particle size and the average size of the prior  $\beta$ -phase grains. Larger  $\alpha$ -phase particle and prior  $\beta$ -phase grain sizes (associated with prolonged material exposure to high temperatures approaching but remaining lower than the upper beta-transus line) generally compromise both the material strength and ductility, making the HAZ the weakest section in the FSW joint.

#### 5.1.2 Stir zone (weld nugget)

The typical room-temperature microstructure of the material residing in this FSW zone consists of  $\alpha + \beta$ -lamellar colonies, suggesting that the material was exposed (for a sufficient amount of time) to temperatures exceeding the upper beta-transus line. The microstructure parameter controlling the material strength and ductility in this region is the average size of the  $\alpha + \beta$ -lamellar colonies. Again, coarser microstructure resulting from a prolonged high-temperature exposure (e.g. associated with a lower tool travel-to-rotational speed ratio) and a lower rate of cooling to room temperature (e.g. as found in thicker welds) gives rise to a simultaneous loss in strength and ductility of the material. However, even in thick welds, it is generally observed in the case of flaw-free FSW joints (the case analysed in the present work) that the strength and ductility of the material in the stir zone are superior to their counterparts in the HAZ.

Based on the discussion presented above, the problem of relating the FSW process parameters to the structural performance of an FSW weldment reduces to the problem of establishing correlations between the FSW process parameters and the HAZ-material microstructure/properties alone. Since microstructure/property changes in the HAZ are only the result of exposure of the material residing in this zone to high temperatures (i.e. plastic deformation has no effect in this region), the reduced problem, while still challenging, is considerably more tractable. That is, one needs to consider only the effect of temperature history of the material residing in this zone on its microstructure/properties. It should be noted that the temperature history of the material residing in the HAZ can be readily extracted from the results file generated during the aforementioned computational analysis of the FSW process. However, modelling of the material microstructure evolution (from the known initial microstructure) subjected to a given temperature history and the associated evolution in the material properties, two quite challenging problems, need to be addressed. The problems of microstructure and property evolution are handled in section 5.2.

### 5.2 Prediction of microstructure/property evolution

Before dealing with the problem of modelling the evolution of material microstructure/properties during FSW, it should be recalled that the controlling microstructure parameters in the HAZ are the globular  $\alpha$ -phase particle size and the prior  $\beta$ -phase grain size (while in the stir zone the dominant microstructure parameter is the  $\alpha + \beta$ -lamellar colony

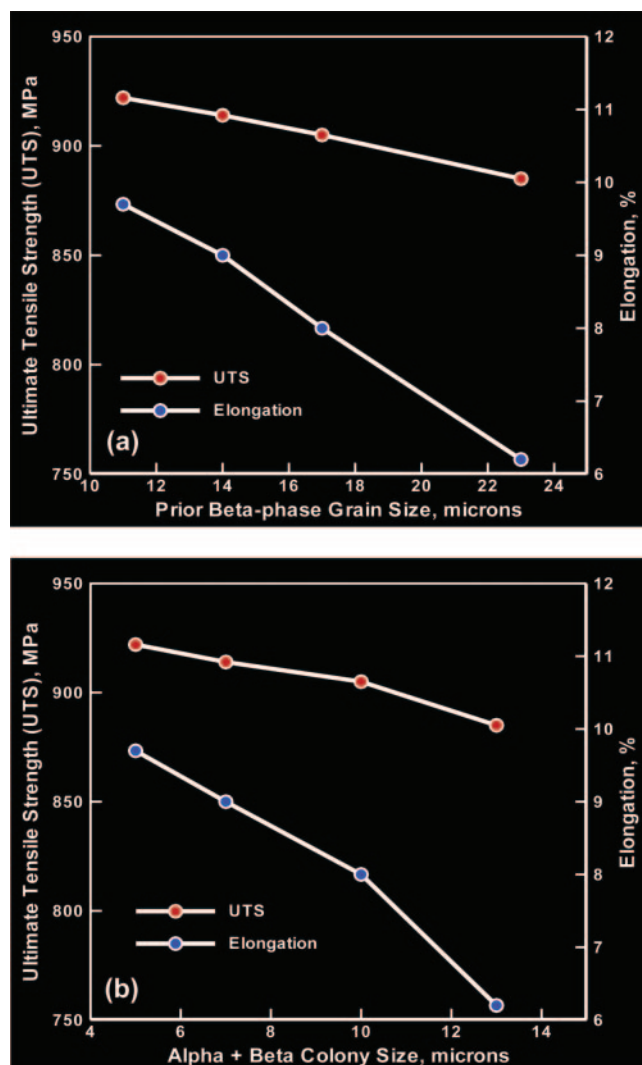


**Fig. 8** Correlations between the ultimate tensile strength/ductility and the dominant microstructural parameter in the case of: (a) the HAZ material, in which the prior  $\beta$ -phase grain size plays a dominant role; (b) the stir-zone material, in which the  $\alpha + \beta$ -colony size plays a dominant role

size). In the present work, the correlations between the ultimate tensile strength/ductility and the dominant microstructural parameter as reported in reference [16] are used. These correlations are depicted graphically in Figs 8(a) and (b) for the HAZ and the stir-zone materials, respectively. The analysis presented below deals only with the HAZ material since this portion of the weld material has the most inferior properties and, hence, controls the structural response of the weld.

It should be also noted that the work reported in reference [23] established a correlation between the HAZ-material ultimate tensile strength, UTS, and its Vickers hardness, HV, as:  $UTS \text{ (MPa)} = 3.27 \times HV \text{ (kgf/mm}^2\text{)}$ . Furthermore, the spatial distribution of the Vickers hardness over a transverse section of the weld

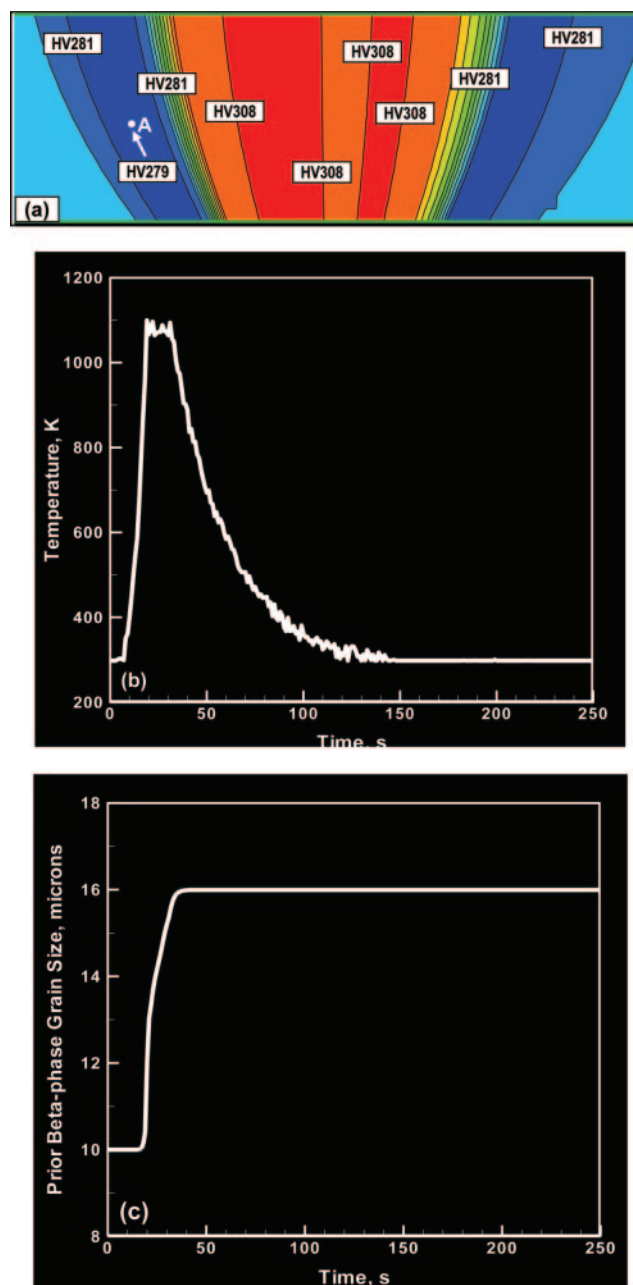


**Fig. 9** (a) Spatial distribution of Vickers hardness over a transverse section of an FSW joint; (b) computed temperature history of the material point associated with the HAZ location marked A in panel (a); (c) the associated computed temporal evolution of the prior  $\beta$ -phase grain size

for several combinations of the FSW process parameters was reported in reference [20]. An example of these results is displayed in Fig. 9(a). All these findings and correlations provide a unique opportunity to validate the present computational approach which relates the FSW process parameters with the resulting weld microstructure/properties. That is, if the present approach can predict the prior  $\beta$ -phase grain size for an arbitrary material point within the HAZ



and for a given set of FSW process parameters (like the ones associated with Fig. 9(a)), then the corresponding ultimate tensile strength (and ductility) can be obtained from Fig. 8(a) and the associated Vickers hardness can be computed using the aforementioned correlation. Vickers hardness computed in this way can then be compared with its experimental counterpart displayed in Fig. 9(a).

To complete the task described above, however, one must be able to model the evolution of the globular  $\alpha$ -phase particle size and the prior  $\beta$ -phase grain size over an arbitrary temperature history. In other words, one must be able to evaluate the following integral

$$D = D_0 + \int_0^t \dot{D}(T(t), D(t), D_0) dT(t) \quad (1)$$

where  $D$  and  $D_0$  are respectively the final and initial  $\beta$ -phase grain size,  $t$  is time,  $T$  is temperature, and a raised dot is used to denote a time derivative of a quantity.

To derive an expression for the grain-size growth rate, the isothermal grain-growth kinetics law reported in reference [24] was used according to which

$$D(t, T) - D_0 = k(T)t^n \quad (2)$$

where  $k(T) (= k_0 e^{-Q/RT})$  is a temperature-dependent rate constant with  $k_0 = 7.05 \mu\text{m.s}^{-n}$ ,  $Q (= 97 \text{ kJ/mol})$  is the activation energy,  $R (= 8.314 \text{ J/mol.K})$  is the universal gas constant, and  $n (= 0.55)$  is a grain-growth exponent. Using a simple mathematical procedure, the integrated isothermal grain-growth law given by equation (2) is converted into a grain-growth rate equation in the form

$$\dot{D}(T, D, D_0) = k(T)^{1/n} (D - D_0)^{(n-1)/n} n \quad (3)$$

Once equation (3) is substituted into equation (1) and  $T$  is replaced by the temperature history  $T(t)$ , the final grain size can be computed by numerically solving the resulting integral equation. Since the grain-size growth rate is a function of the current grain size, the integration has to be carried out sequentially starting with the first time increment.

An example for the application of the aforementioned procedure is discussed in the remainder of this section. First, an arbitrary location A is selected within the HAZ in Fig. 9(a). Figure 9(a) shows a contour plot of the distribution of Vickers hardness over the transverse section of a Ti-6Al-4V FSW joint as reported in reference [20]. Location A in Fig. 9(a) is associated with a Vickers hardness level of HV279. The present computational approach is next used to compute the thermal history of the material point corresponding to location A in Fig. 9(a). It should be recalled that due to the use of the ALE algorithm,

there is a distinct difference between a spatial location and a material point. That is, different material points reside at different times at the same spatial location within the computational domain. The computed temporal evolution of the temperature associated with location A in Fig. 9(a) is depicted in Fig. 9(b). When this temperature history is used in conjunction with equations (1) and (3), the temporal evolution of the globular  $\alpha$ -phase particle size and prior  $\beta$ -phase grain size is obtained, Fig. 9(c). The final  $\beta$ -phase grain size ( $\sim 16 \mu\text{m}$ ) obtained in Fig. 9(c) is then used in conjunction with Fig. 8(a) to determine the corresponding material ultimate tensile strength,  $\text{UTS} = 908 \text{ MPa}$ . The aforementioned UTS versus HV correlation then suggests that the corresponding material Vickers hardness is  $\sim 277.7$ . This value is very close to the experimentally measured Vickers hardness value of HV279. Since similar findings were obtained in the case of other combinations of FSW process parameters, one may conclude that the present computational approach accounts reasonably well for the established effects of the FSW process parameters on the material microstructure/properties. This finding is quite encouraging, suggesting that the present computational approach may be used to guide the selection of FSW process parameters in order to optimize the structural performance of FSW welds (at least when they are controlled by the HAZ-material microstructure/properties).

As stated earlier, the main goal of the present work was to develop and validate a mainly computational approach to predicting microstructure and property evolutions in different FSW weld zones and correlate these evolutions with the attendant FSW process parameters. As demonstrated earlier in this section, to achieve this goal a number of published experimental results pertaining to material microstructure and properties had to be utilized. Also, it was stated that an experimental study complementary to the present computational investigation is underway. As per the suggestion of one of the reviewers of the manuscript, an example of the experimental evidence for microstructural coarsening in the HAZ is provided in Figs 10(a) and (b). The scanning electron micrographs shown in Fig. 10 depict a HAZ location adjacent to the stir zone which undergoes major microstructural coarsening (and, hence, strength/hardness degradation) during FSW. It should be noted that the results displayed in Figs 10(a) and (b) provide evidence only for coarsening of the  $\alpha$ -phase (the dominant phase in Ti-6Al-4V) while the associated proof for coarsening of prior  $\beta$ -phase grains is not that evident. Nevertheless, it should be noted that microstructural coarsening tends to encompass all the key microstructural features, so that direct evidence for  $\alpha$ -phase coarsening suggests that

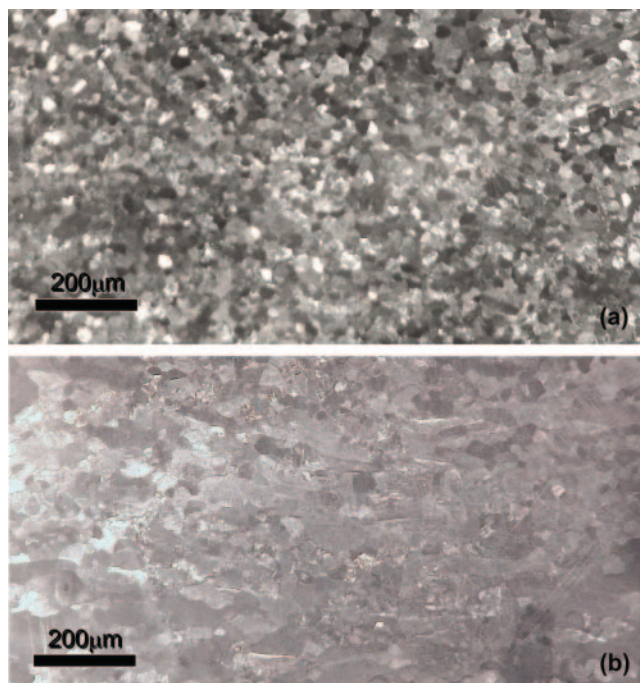


**Fig. 10** Scanning electron micrographs of Ti-6Al-4V: (a) as-received condition; (b) a HAZ location bordering with the stir zone. In both micrographs, the visible microstructural features correspond to the globularized  $\alpha$ -phase particles

prior  $\beta$ -phase coarsening is quite likely. An effort will be made in the authors' ongoing experimental study to obtain direct evidence for coarsening and this will be reported in a future communication.

## 6 SUMMARY AND CONCLUSIONS

Based on the work presented and discussed in the current paper, the following main summary remarks and conclusions can be made.

1. A brief overview is provided of the key physical metallurgy and FSW behaviour of Ti-6Al-4V, a commercially available titanium alloy.
2. Based on the available results in the literature, it is concluded that the HAZ contains the most inferior properties and that it controls the overall structural performance of the weld.
3. A mathematical model is developed and parameterized for temporal evolution of the globular  $\alpha$ -phase particle size and the prior  $\beta$ -phase grain size during the FSW process. This model is next combined with the well-established property versus microstructure correlations in Ti-6Al-4V to predict computationally mechanical properties within the HAZ.
4. The results obtained are found to be in reasonably good agreement with their experimental coun-

terparts and suggest that the present computational approach may be used to guide the selection of FSW process parameters in order to optimize the structural performance of FSW joints (at least while they are controlled by the HAZ-material microstructure/properties).

## ACKNOWLEDGEMENT

The material presented in this paper is based on work supported by the US Army/Clemson University Cooperative Agreements W911NF-04-2-0024 and W911NF-06-2-0042 and by the Army Research Office sponsored grant W911NF-09-1-0513.

© Authors 2011

## REFERENCES

- 1 Thomas, W. M., Nicholas, E. D., Needham, J. C., Murch, M. G., Temple-Smith, P., and Dawes, C. J. Friction stir butt welding, International Patent Application No. PCT/GB92/02203, 1991.
- 2 Liu, H., Fulii, H., Maeda, M., and Nogi, K. Tensile properties and fracture locations of friction-stir welded joints of 6061-T6 aluminum alloy. *J. Mater. Sci. Lett.*, 2003, **22**, 1061–1063.
- 3 Lee, W. B., Lee, C. Y., Chang, W. S., Yeon, Y. M., and Jung, S. B. Microstructural investigation of friction stir welded pure titanium. *Mater. Lett.*, 2005, **59**, 3315–3318.
- 4 Thomas, W. M. and Nicholas, E. D. Friction stir welding for the transportation industries. *Mater. Des.*, 1997, **18**, 269–273.
- 5 Su, J. Q., Nelson, T. W., Mishra, R., and Mahoney, M. Microstructural investigation of friction stir welded 7050-T651 aluminum. *Acta Mater.*, 2003, **51**, 713–729.
- 6 Frigaard, O., Grong, Ø., and Midling, O. T. A process model for friction stir welding of age hardening aluminum alloys. *Metall. Mater. Trans. A*, 2001, **32**, 1189–1200.
- 7 Mahoney, M. W., Rhodes, C. G., Flintoff, J. G., Spurling, R. A., and Bingel, W. H. Properties of friction-stir welded 7075 T651 aluminum. *Metall. Mater. Trans. A*, 1998, **29**, 1955–1964.
- 8 Rhodes, C. G., Mahoney, M. W., Bingel, W. H., Spurling, R. A., and Bampton, C. C. Effect of friction stir welding on microstructure of 7075 aluminum. *Scripta Mater.*, 1997, **36**, 69–75.
- 9 Liu, G., Murr, L. E., Niou, C. S., McClure, J. C., and Vega, F. R. Microstructural aspects of the friction-stir welding of 6061-T6 aluminum. *Scripta Mater.*, 1997, **37**, 355–361.
- 10 Grujicic, M., Arakere, G., Yen, C.-F., and Cheeseman, B. A. Computational investigation of hardness evolution during friction-stir welding of AA5083 and AA2139 aluminum alloys. *J. Mater. Des. Applic.*, 2010. DOI: 10.1007/s11665-010-9741-y.

- 11 **Ramirez, A. J.** and **Juhas, M. C.** Microstructural evolution in Ti-6Al-4V friction stir welds. *Mater. Sci. Forum*, 2003, **426–432**, 2999–3004.
- 12 **John, R., Jata, K. V.,** and **Sadananda, K.** On the residual stress field in the aluminum alloy FSW joints. *Int. J. Fatigue*, 2003, **25**, 939–948.
- 13 **Lee, W. B., Lee, C. Y., Chang, W. S., Yeon, Y. M.,** and **Jung, S. B.** Microstructural investigation of friction stir welded pure titanium. *Mater. Lett.*, 2005, **59**, 3315–3318.
- 14 **Reynolds, A. P., Hood, E.,** and **Tang, W.** Texture in friction stir welds of Timetal 21S. *Scripta Mater.*, 2005, **52**, 491–494.
- 15 **Fonda, R. W., Knipling, K. E., Feng, C. R.,** and **Moon, D. W.** *Friction stir welding and processing IV*, 2007, pp. 295–301 (TMS, Warrendale, Pennsylvania, USA).
- 16 **Zhang, Y., Sato, Y. S., Kokawa, H., Park, S. H. C.,** and **Hirano, S.** Microstructural characteristics and mechanical properties of Ti-6Al-4V friction stir welds. *Mater. Sci. Engng A*, 2008, **485**, 448–455.
- 17 **Liu, H. J., Zhou, L.,** and **Liu, Q. W.** Microstructural characteristics and mechanical properties of friction stir welded joints of Ti-6Al-4V titanium alloy. *Mater. Des.*, 2010, **31**, 1650–1655.
- 18 **Grujicic, M., He, T., Arakere, G., Yalavathy, H. V., Yen, C.-F.,** and **Cheeseman, B. A.** Fully coupled thermo-mechanical finite element investigation of material evolution during friction-stir welding of AA5083. *Proc. IMechE, Part B: J. Engineering Manufacture*, 2010, **224** (4), 609–625. DOI: 10.1243/09544054JEM1750.
- 19 **Grujicic, M., Arakere, G., Yalavathy, H. V., He, T., Yen, C.-F.,** and **Cheeseman, B. A.** Modeling of AA5083 material-microstructure evolution during butt friction-stir welding. *J. Mater. Engng Perform.*, 2010, **19**, 672–684. DOI: 10.1007/s11665-009-9536-1.
- 20 **Edwards, P. D.** and **Ramulu, M.** Investigation of microstructure, surface and subsurface characteristics in titanium alloy friction stir welds of varied thickness. *Sci. Technol. Weld. Join.*, 2009, **14**, 476–483.
- 21 **Anon.** ABAQUS Version 6.8–1, User Documentation, Dassault Systems, Rhode Island, USA, 2008.
- 22 **Johnson, G. R.** and **Cook, W. H.** A constitutive model and data for metals subjected to large strains, high strain rates and high temperatures. In *Proceedings of the 7th International Symposium on Ballistics*, The Hague, The Netherlands, 3–10 April 1983.
- 23 **Gupta, M.** and **Srivatsan, T. S.** Interrelationship between matrix microhardness and ultimate tensile strength of discontinuous particle-reinforced aluminum-alloy composites. *Mater. Lett.*, 2001, **51**, 255–261.
- 24 **Gil, F. J.** and **Planell, J. A.** Grain growth kinetic of near alpha titanium alloys. *Mater. Sci. Lett.*, 2000, **19**, 2023–2024.